Fabrication and Analysis of Ion-Engineered ZnO Device Structures for Optoelectronic Applications

Fareeha Younus [ORCID], Ahmed Shuja [ORCID], and Muhammad Ali [ORCID]

Abstract—**ZnO-based devices are highly promising for applications involving light-matter interaction. This work explores the impact of light-matter interaction on ion-induced ZnO structures and their respective energy band profiles. Incorporation of various ions, (Au^+, B^+, Cu^+, P^+) into the ZnO lattice, deposited via magnetron sputtering on an n-type Si substrate was investigated in detail. To assess the impact of these ions on the ZnO surface, monte-carlo simulations at low energies were performed and optimal ion dose and energy conditions were determined. The resulting post-fabrication devices underwent comprehensive structural, morphological, optical, and electrical diagnostics. X-ray diffraction (XRD) analysis confirmed the well-maintained crystal structure of the ZnO lattice along the $<100>$ direction for all implant sequences. Notably, the gold (Au^+) implant exhibited the highest light extinction into the ZnO matrix, as indicated by the extinction coefficient and refractive index data. This observation suggested that Au^+ implantation could effectively generate electron-hole pairs. The photovoltage and dark/light current measurements provided further evidence of enhanced light-matter interactions and responsivity in the Au^+-implanted devices owing to light-induced currents. Furthermore, the energy bands of all implant cases were profiled by Charge Deep Level Transient Spectroscopy (Q-DLTS) measurements by evaluating discrete energy states within the ZnO lattice.**

Index Terms—**Extinction coefficient, ion radiations, photodetection, QDLTS, responsivity, transients of photovoltage.**

I. INTRODUCTION

OPTOELECTRONIC devices such as lasers, light-emitting diodes (LEDs), and photo detectors, have revolutionized various technological applications by leveraging the control and manipulation of electromagnetic radiations [1]. In recent years significant progress has been made in the development of wide band-gap based semiconductor optoelectronic devices aiming to improve device parameters, such as efficiency, detection range, and gains [2]. Zinc oxide (ZnO) has gained widespread attention in this context due to its inherent advantages, including wide band gap, high carrier mobility, high stability, radiation tolerance, and large excitation energy (60 meV) at room temperature [3], [4]. These properties make ZnO highly desirable for optoelectronic applications, as it exhibits strong light-matter interactions and sustains its excitons at room temperature, enabling strong electromagnetic spectrum emission capabilities [1], [5].

However, there are certain limitations and challenges, such as the adsorption of oxygen molecules on the surface of ZnO, narrow absorption range, and p-type conductivity [6], [7], [8]. These issues have led to slower response time and high switching times in photodetectors fabricated from ZnO limiting their bandwidth. To overcome these challenges and enhance the performance of ZnO-based photodetectors, researchers have explored various approaches, such as device design engineering, novel fabrication techniques, and improvements in device structures.

Among these efforts, literature shows numerous studies related to the tailoring of ZnO band gap by incorporating multi-component alloys, such as ZnO ternary alloys (e.g., ZnOS) and ZnO quaternary alloys (e.g., BeMgZnO) [4], [9], [10], [11], [12], [13]. The optical band gap plays a crucial role in applications like photodetectors, light emitters, and lasers, making band gap tailoring essential for wavelength modulation. Doping ZnO with external species has been a successful approach for modulating the band gap, and previous studies have investigated the effects of incorporating species like Cobalt (Co), Copper (Cu), and Phosphorus (P) into the ZnO matrix during fabrication [8], [9], [10]. The introduction of external species through doping can lead to changes in the adsorption and extinction coefficients, resulting in a range of localized states and structural disorders [13].

Radiation-induced ion implantation offers the flexibility of modifying material properties and achieving optoelectronic activity within the ZnO band structure by establishing the right routines [14], [15]. This technique has been widely employed in the development of semiconductor devices and structures [16], [17], [18], [19]. However, ion implantation can introduce complex defects that significantly impact the electrical and optical properties of the targeted device, because they can act as recombination centers, leading to substantial changes in the charge carrier profiles of the material [20], [21], [22]. Understanding the complex nature of intrinsic and impurity-related defects is crucial for comprehending and reconciling the electrical behavior of ZnO-based devices.

In this work, we present a comprehensive study of the ion-implanted ZnO deposited on an n-type Si substrate through the Magnetron sputtering technique. The selected ions (B, Cu, P, Au, and Au & B) introduce defect states within the crystal structure of ZnO, thereby influencing the structural, optical, and electrical properties of the devices. We systematically examined and reported various microstructural (crystallographic orientation and
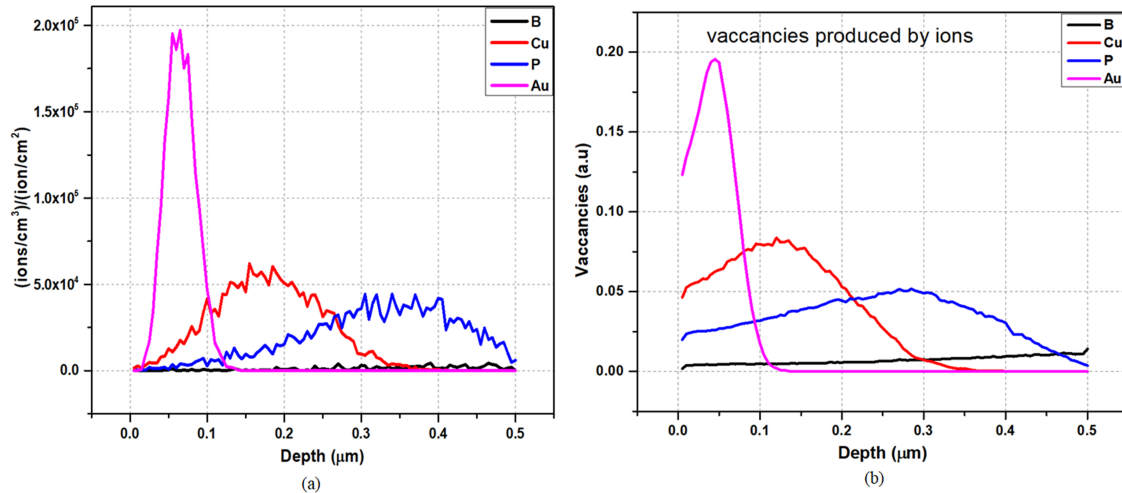
Fig. 1.   (a) Range profile (b) vacancy profile of B, Cu, P, and Au implanted devices in SRIM/TRIM.

grain size), optical (transmittance, optical band gap, refractive index, dielectric constant, photoluminescence), and electrical (current-voltage characteristics, transients of photovoltage, the kinetics of dark and light current, numerical gains and deep level charge transients) parameters of the deposited and implanted ZnO thin films.

By investigating these parameters, we aim to gain insights into the potential improvements and reliability enhancements of ZnO-based optoelectronic devices.

II. Experimental Section

A. Device Design

The device design process involved the utilization of Stopping and Range of Ions in Matter (SRIM/TRIM) and Surrey University Sputter Profile Resolution from Energy Deposition (SUSPRE) software tools. SRIM/TRIM, Monte Carlo-based simulation software, was employed for the ion implantation routines. By using this tool ion penetration depth and resulting damage distribution within the device structure can be predicted. SUSPRE on the other hand, provided valuable insights by calculating the first two moments of the Gaussian distribution, allowing the selection of an optimal dose for the actual implantation process.

Through multiple simulation runs and careful analysis of the results, specific ion species were chosen for the implantation process. Boron (B^+), Copper (Cu^+), Phosphorus (P^+), Gold (Au^+), and a special case of Au^+&B^+ were selected, considering their respective implant energies of 400 keV, at a device thickness of 500 nm. The energy schedules and ion species were carefully chosen to ensure that the resulting profile remained within the desired limits of the device, without penetrating the substrate. This approach aimed to prevent the leakage paths that could compromise the overall performance of the optoelectronic devices.

The results of the range profile concerning the depth of the device, after device designing, are shown in Fig. 1(a) while (b) shows the vacancy profile. It is evident that, gold being

the heaviest (196.7) has traversed only a short distance within the device thickness, on the other hand, boron ions, seem to traverse a far long distance, giving the widest straggle. Au^+ ions having the largest mass produce the highest vacancies, as compared to others, as shown in Fig. 1(b). Extensive analysis was conducted on the simulation data, to ensure the precise placement of the injected ions within the thickness of the device layer. Additionally, great attention was given to preventing the penetration of implanted ions beyond the substrate (Si) layer. It was crucial to ensure that the concentration of ions reached zero at a depth of 5000 Å, effectively confining the ion implantation within the ZnO layer without adversely affecting the underlying substrate.

By thoroughly analyzing and optimizing the simulation data, we were able to establish the ideal conditions for the implantation process. This meticulous approach guaranteed the proper positioning of the ions within the device layer, thereby maximizing the potential for desired light-matter interactions while maintaining the structural integrity of the optoelectronic devices.

B. Fabrication of ZnO Thin Film

The fabrication routines were meticulously designed based on the results obtained from the device design section. The target thin film of ZnO was deposited on both silicon and glass substrates using the DC Magnetron Sputtering (MS) technique. To ensure a homogenous interface, n-type silicon (Si) wafer with a thickness of approximately 300 μm and doped with arsenic, exhibiting <111> orientation, was chosen for the deposition of the ZnO thin film. The Si wafer underwent standard cleaning protocols, including a splash of acetone and Iso-Propyl Alcohol (IPA), followed by deionized water rinsing. Nitrogen gas was then used for a final cleaning step. In parallel, a transparent glass strip was also subjected to the same cleaning process.

Both silicon and glass substrates were cleaved and placed into the magnetron sputtering chamber. The deposition process was carried out at room temperature (21 °C), using a 3-inch
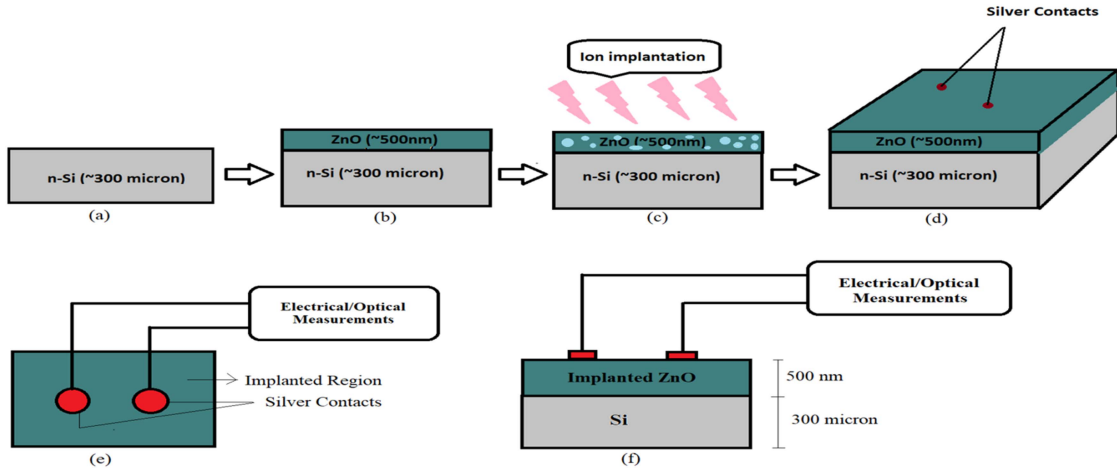
Fig. 2. Fabrication of ZnO-based devices and placement of silver contacts (a) silicon substrate, (b) ZnO growth, (c) ion Implantation, (d) cross-sectional view, (e) top view, (f) side view.

diameter ZnO target composed of 99.9% pure ZnO disk and having a density of 5.61 g/cm^3. A DC magnetron sputtering system was employed for the deposition of the ZnO thin film. The base pressure in the chamber was set to 6.3 mPa, with a deposition pressure of 0.16 Pa. The DC used was 350 mA, and the desired film thickness was targeted at 5000 Å.

The deposition rate varied at around 0.4 Å/s, while the argon flow rate was maintained at 22 sccm throughout the deposition process. The deposition rate and film thickness were continuously monitored using a Quartz crystal thickness monitor. To ensure uniform thickness across the entire deposited thin film, the substrate holder was rotated at a constant speed of 15 rpm. Additionally, the sputtering angle was set as 45°, and the source to target distance was maintained at 6 cm. The stepwise procedure for the fabrication of ZnO devices is depicted in Fig. 2.

After the completion of the fabrication process, a set of the as-grown ZnO thin film was retained for characterization in its pristine state. The remaining samples were subjected to ion implantation using a 5 MV Tandem (pelletron) accelerator at the National Center of Physics (NCP) in Islamabad. The chosen ions for implantation included Boron (B$^+$), Copper (Cu$^+$), Phosphorus (P$^+$), Gold (Au$^+$), and Au$^+$ & B$^+$ both.

The ion dose and energy parameters for the implantation process were determined based on the simulation results obtained earlier. It was decided to implant the ions at a dose of approximately 1×10^{14} ions/cm^2 and an energy of 400 keV. These parameters were carefully selected to ensure that the resulting implantation-induced defects and modification remain within the desired range, allowing for the desired modifications to the optoelectronic properties of the ZnO thin films.

III. RESULTS AND DISCUSSION

Following the device design and fabrication stages, a comprehensive characterization of both the as-grown and implanted ZnO devices was conducted. The characterization included surface morphology analysis using Atomic Force Microscopy (AFM), structural analysis using X-Ray Diffraction (XRD), optical analysis using Photoluminescence (PL) and Ellipsometry, and electrical analysis using various techniques.

For electrical characterization, silver (Ag) contacts with an area of approximately ~ 1 mm^2 were deposited on the devices. The electrical measurements, such as Current-Voltage (I-V) characteristics, Charge Deep Level Spectroscopy (Q-DLTS), Transients of Photo Voltage (TPV), and Kinetics of Dark and Luminous currents, were performed using the Automatic System for Material Electro-physical Characterization (ASMEC) system. These measurements provide valuable insights into the electrical behavior, carrier dynamics, and defect levels in the ZnO devices.

A. Surface Morphology

Surface morphology analysis using the AFM technique was conducted to examine the pristine (as-grown) and implanted devices at room temperature. The AFM images are presented in Fig. 3.

Fig. 3(a) shows the AFM image of the as-grown ZnO thin film. It can be observed that the surface is smooth, indicating a well-controlled deposition process during magnetron sputtering.

Comparing the surface morphology of the Cu$^+$ and Au$^+$-implanted devices, as shown in Fig. 3(b) and (c) respectively, it can be noted that they exhibit similar surface features. The similarity may be attributed to the comparable masses of Cu$^+$ and Au$^+$ ions, resulting in similar effects on the surface morphology of the ZnO thin film. In contrast, Fig. 3(d). reveals that the P$^+$-implanted device displays distinct surface morphology compared to the as-grown and metal-implanted devices. The resulting granular structure is visible, suggesting that the incorporation of phosphorus ions during ion implantation introduces significant changes to the surface morphology. These variations in surface morphology are expected to have an impact on the electro-optical characteristics of the devices, which will be
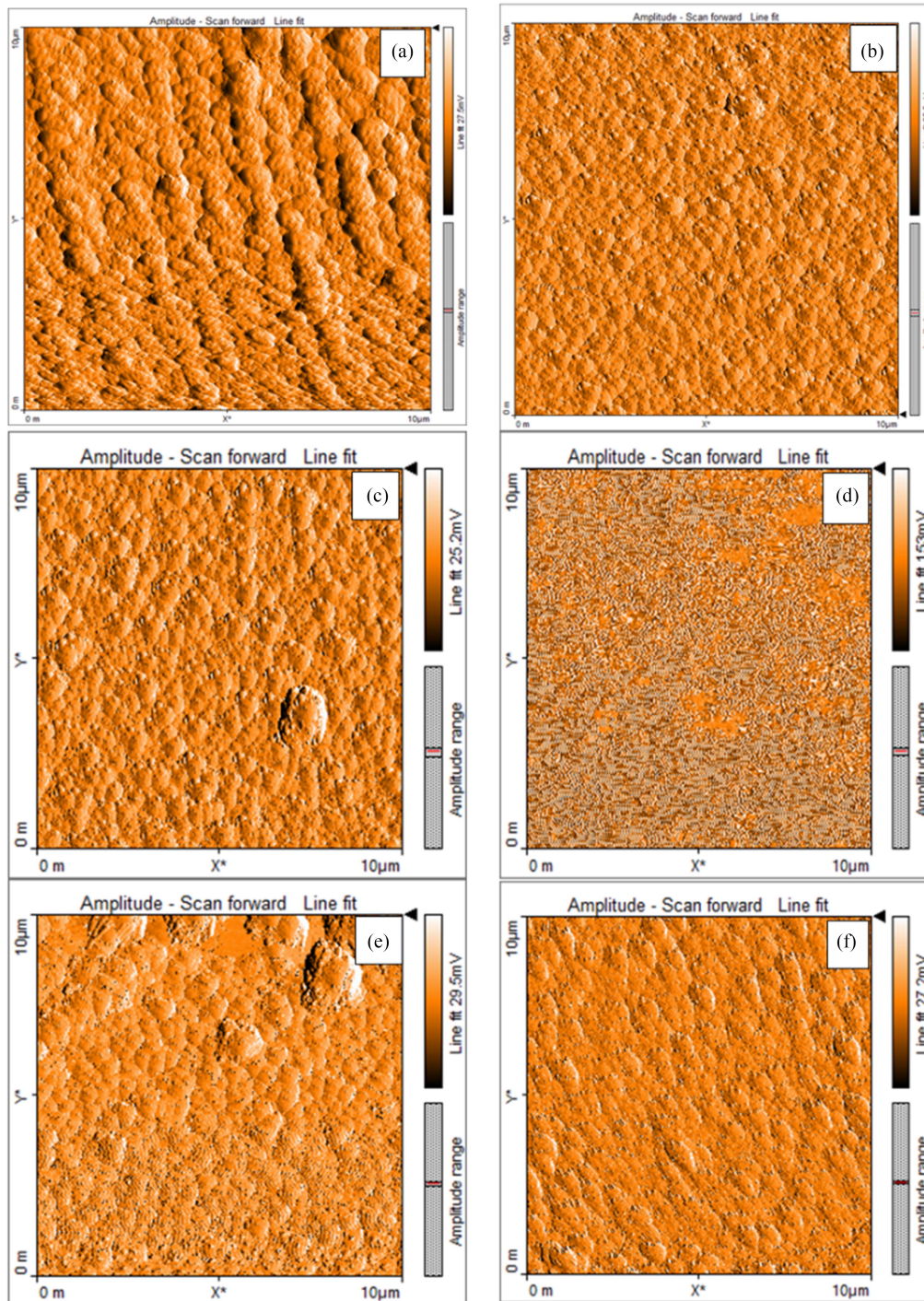
Fig. 3. Surface topography using AFM technique (a) as-grown, (b) B implanted, (c) Cu implanted, (d) P implanted, (e) Au implanted, (f) multi implant (Au&B) devices.

further discussed in the upcoming sections. The RMS roughness was also measured and reported in Table I.

B. Structural Analysis

The structural morphology of the as-grown and implanted ZnO thin films was studied using an X-ray diffractometer (PAN analytical X'pert pro) with Cu-Kα radiation (λ = 1.5406 Å).

The scan range for the XRD analysis was set between $10° \leq 2\theta \leq 65°$. Fig. 4 displays the XRD spectra of the as-grown and implanted ZnO thin films. The observed peak positions in all devices, specifically at $2\theta = 30°$ and, $45°$, correspond to the (100) and (102) diffraction planes, respectively. These peak positions align well with the reported values for pure ZnO thin films, indicating that the implanted external species did not significantly alter the original peaks of ZnO. The presence of

TABLE I
RMS ROUGHNESS OF AS-GROWN AND IMPLANTED DEVICES

Sr. No.	Device	RMS Roughness (nm)
1	as grown	19.942
2	B implanted	10.085
3	Cu implanted	10.584
4	P implanted	16.742
5	Au implanted	25.967
6	Au & B implanted	10.137

TABLE II
GRAIN SIZE AND LATTICE STRAIN

Sr. No.	Grain size (nm)	Lattice strain x10^{-3}
1	58.35	3.12
2	67.51	2.58
3	59.06	2.79
4	68.80	2.07
5	63.35	2.23
6	54.23	2.78
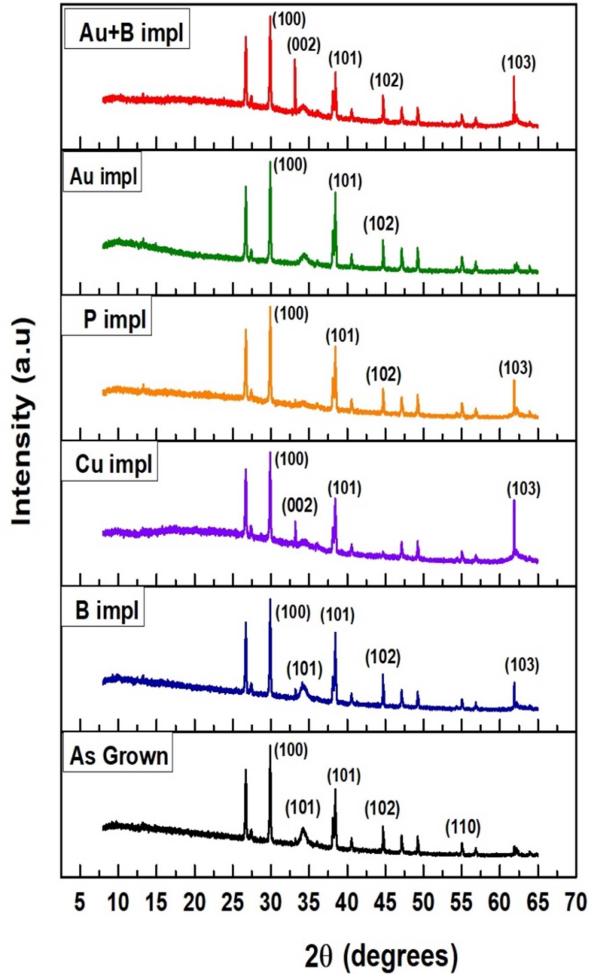
Fig. 4. XRD spectra of as-grown and implanted ZnO devices.

Fig. 5. Transmission spectra of ZnO.

grain size (D) to the X-ray wavelength (λ), the full-width half maximum (β), and the diffraction angle (θ).

$$D = \frac{0.9\lambda}{\beta \cos\theta} \tag{1}$$

Lattice strain was calculated using "(2)" [28].

$$\text{Lattice Strain} = \frac{\beta}{4\tan\theta} \tag{2}$$

Table II presents the average crystal size and average lattice strains of all the devices. It can be observed that lattice strain decreases with the incorporation of external species into the ZnO device matrix. The grain size, on the other hand, increases slightly. These findings are consistent with previous studies [29].

C. Optical Analysis

The optical properties of the deposited and implanted ZnO devices were analyzed using spectroscopic ellipsometry. The transmission spectra of the ZnO thin film on a glass substrate were measured in the range of 320 to 850 nm using a SENTECH-800 ellipsometer. The glass substrate was deliberately chosen to gauge the transmission spectra because the transmission of the glass slide is already 100%, thus, it only provides the transmission of deposited ZnO. Fig. 5 presents the obtained spectra, showing the transmittance of light through the ZnO thin film.

these peaks confirms the hexagonal crystal structure of ZnO, oriented along the c-axis and perpendicular to the substrate plane, as reported in previous studies [23], [24]. The sharpness of the peaks further suggests the good crystalanity and single crystal behavior of ZnO devices [25], [26], [27]. Additionally, a peak at $2\theta = 26.6°$ is observed in all devices, which may be attributed to the presence of oxide impurities such as SiO_2 [23]. Hence, the implanted external species did not affect the original peaks of ZnO, significantly. To determine the grain size of the devices, Scherer's formula [28] was employed, which relates the
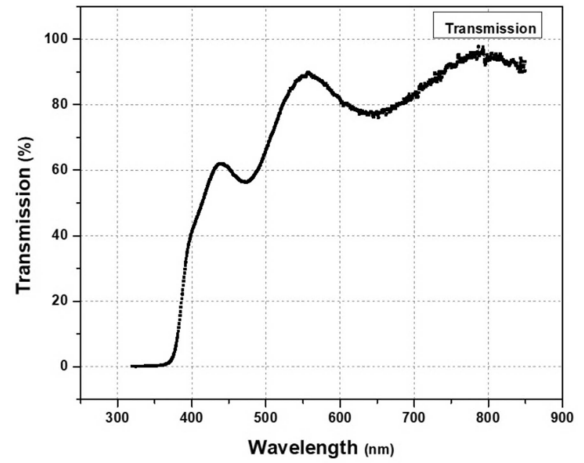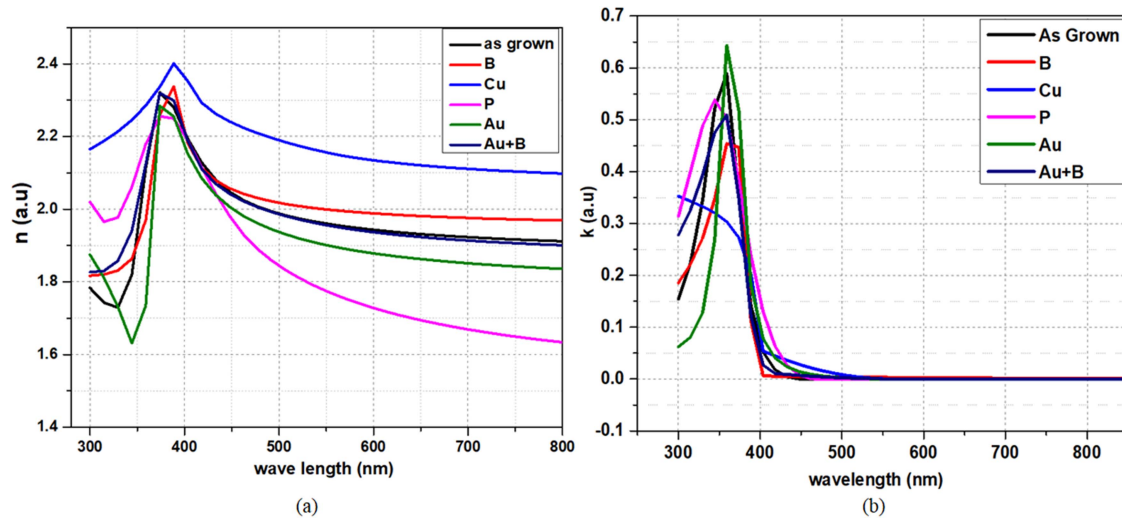
Fig. 6.   (a) Refractive Index (n), (b) absorption coefficient (k) of as-grown and implanted devices.

It can be observed that more than 60% of transmittance occurs at a wavelength of 500 nm, corresponding to the visible range, while 40% of the incident light is transmitted at 400 nm, indicating that the ZnO film exhibits some level of absorption in the visible region. In the UV region (λ<360 nm), the incident light is completely absorbed by the ZnO thin film. This behavior is consistent with previous studies [30], [31], [32]. However, the extent of transmission through ZnO in the visible range varies from 50% to 95%. This results in lesser electron-hole pair generation when subjected to visible light. The said extent has also been investigated in later sections, at length.

To further analyze the optical properties, the refractive index ('n') and extinction coefficient ('k') of all devices under test (DUT) were investigated. These parameters are important for understanding the reduction in the speed of light within the material (n) and the absorption of light (k). The Tauc Lorentz model was used to fit the ellipsometry data and to obtain the 'n' and 'k' spectra for the as-grown and implanted devices, as shown in Fig. 6. It is observed in Fig. 6(a) that the Cu^+-implanted device has the highest refractive index of 2.4 at the wavelength of 388.59 nm followed by B^+ implanted (2.34). The P^+ implanted device has the lowest "n" (2.26). Hence the P^+-implanted device shows the highest speed of light within the active layer of the device. A higher refractive index indicates a slower speed of light within the material and larger scattering events at a given wavelength.

The extinction coefficient 'k' is the imaginary part of the refractive index, and is a function of the absorption coefficient and wavelength. Fig. 6(b) shows the k versus λ spectrum of DUTs in a given wavelength range. It can be observed that extent of light absorbed is the highest in the Au^+ implanted device at a wavelength of 350 nm, sharply decreasing thereafter. The Cu^+ implanted device has shown the least absorption as compared to the other devices, but its absorption decreases smoothly. These variations in absorption behavior can be attributed to factors such as the presence of external species and temperature effects on nanoparticle size [31]. The optical band gap, which represents

the threshold energy for photon absorption was determines using the Tauc's "(3)" [33].

$$\alpha\hbar\upsilon = B(\hbar\upsilon - Eg)^{\frac{1}{2}} \tag{3}$$

Where 'α' is the absorption coefficient, '$\hbar\upsilon$' is photon energy, 'Eg' is the optical band gap and 'B' is a constant depending upon the probability of absorption and refractive index of the material. Fig. 7 shows the optical band gap determination based on the linear portion of the $(\alpha\hbar\upsilon)^2$ verses ($\hbar\upsilon$) plot. It can be seen in the Fig. that the injected external species lowered the band gap of the pristine ZnO. It means that we need less amount of energy for optoelectronic devices in implanted devices as compared to un-implanted ones The Cu^+-implanted device exhibited the lowest band gap, followed by P^+-implanted and Au^+-implanted devices. The double-implanted device (Au^+&B^+) resulted in an optical band gap of 3.17 eV, closer to that of B^+-implanted alone. The modulation of the band gap by incorporating specific ion species demonstrates the potential for tailoring the optical properties of ZnO. Previous studies have also reported the influence of growth conditions and doping on the band gap of ZnO, highlighting the versatility of ZnO for various optoelectronic applications [30], [31], [32]. Madhuri Mishra et al. studied the optical properties of ZnO after phosphorus doping. Their study reveals that phosphorus results in shallow-level acceptors with free electron to acceptor level transition at 3.31 eV [34]. Photoluminescence characterization of the ZnO devices was performed using a photoluminescence spectroscope with a He-Cd laser emitting at a wavelength of 325 nm. The scan was done within the given wavelength range (300 nm to 600 nm). The measurements were carried out at a cryogenic temperature of liquid nitrogen ($-196\,°C$) to minimize thermal noise and freeze out thermal vibrations. The obtained results are shown in Fig. 8. It is evident from the figure that the as-grown device exhibits luminescence in the UV range, specifically at a wavelength of 367 nm, indicating the deposition of high- quality ZnO thin film on the Si substrate. Analysis of the implanted devices shows
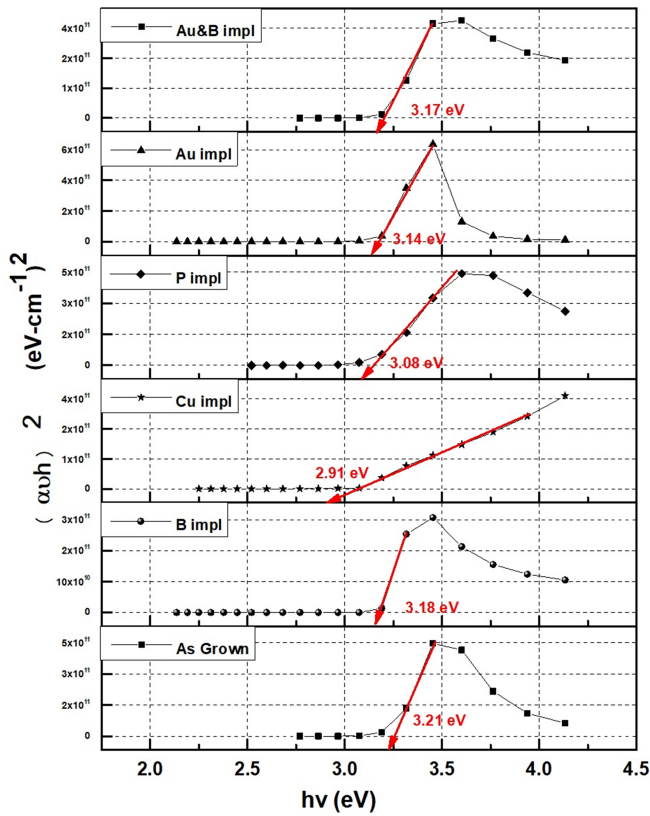
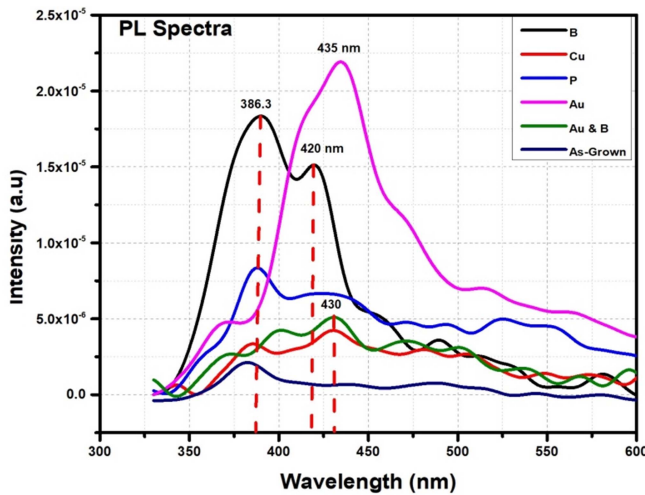Fig. 7. Optical band gap determination from tauc's equation.

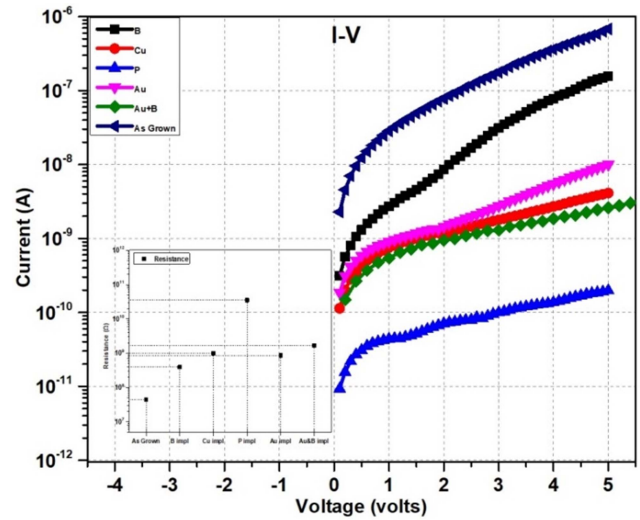Fig. 8. Photoluminescence spectra of as-grown and implanted devices.

Fig. 9. Current-voltage characteristics of as-grown and implanted devices.

that the photoluminescence spectra of ZnO can be influenced by temperature and defects introduced during growth or due to external species [30]. Different emission bands may arise depending on defect levels. The recombination of free excitons typically results in near-band edge (NBE) emission in the UV range, while intrinsic defects and those caused by foreign species can lead to emission in the visible region [35], [36]. The literature suggests various theories for visible light emission in ZnO. Copper-implanted ions, for example, can induce transitions from shallow donors to deep acceptors [37]. Karali et al. reported that copper ions may replace zinc in the host lattice, resulting in visible light emission [38]. Manohar Singh also reported strong violet emissions from copper-doped ZnO, which may be due to zinc vacancies [39].

The Full Width Half Maxima (FWHM) of the peaks reflects the range of wavelengths that can optically activate the devices. As can be seen from the spectrum, all the fabricated devices give a wide range of FWHM for all peaks.

D. Electrical Characterization

The electrical characterization of the fabricated and implanted devices was conducted using Automatic System for Material Electro-physical Characterization (ASMEC). Several measurements were performed, including Current-Voltage (I-V) analysis, Charge Deep Level Transient Spectroscopy (QDLTS), Kinetics of Photo Voltage (TPV), and transients of dark and photocurrents (I_{light}, I_{dark}). The aim was to understand the carrier transport mechanism and investigate the impact of ion implantation on the electrical properties of the devices. The I-V analysis was carried out at a 5 V applied bias to study the current transport behavior.

From the I-V curves shown in Fig. 9, it can be observed that the as-grown device exhibited the highest current, indicating minimal or no damage to the lattice structure. The B^+-implanted device, being the lightest among the implanted species, resulted in less damage and showed higher conductivity. On the other

variations in the peak intensity and emission wavelengths. The Au^+-implanted device exhibits the highest peak intensity at a wavelength of 435 nm. The B^+-implanted devices show two peaks, one at 386.3 nm and another in the visible region at 420 nm.

The double-implanted device (Au^+&B^+) exhibits luminescence at approximately 430 nm, which is close to the wavelength observed in the Au^+-implanted device. The literature reveals

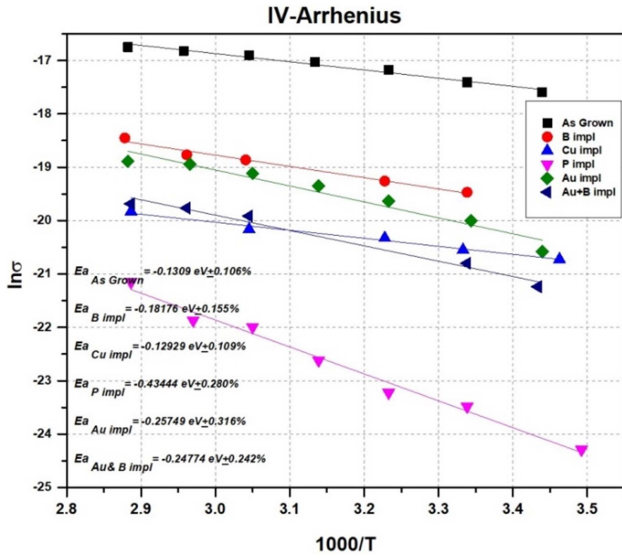Fig. 10. Arrhenius analysis of as-grown and implanted devices.

Fig. 11. Activation energy and resistance of as-grown and implanted ZnO devices.

hand, the P^+-implanted device exhibited the lowest conductivity, likely due to dopant atoms being placed deeper into the surface, contributing fewer carriers [14]. The inset of Fig. 9 confirms this, showing the highest resistance among all devices at approximately $3.54E + 10$ Ω at room temperature. This suggests that the P^+-implanted device is more resistive and experiences more significant physical damage caused by the P^+ ions. Previous research by Madhuri Mishra et al. suggests that ion implantation of phosphorus may promote the generation of point defects, which are related to lattice defects of zero dimensionality [34]. This may reduce the contribution of carriers to charge leakage, resulting in larger resistivity. Carrier mobility exhibited the reverse trend compared to resistance.

To further investigate, the role of ion species and their associated activation energies (Ea), temperature-dependent Arrhenius analysis was performed ranging from room temperature to 350 K.

It is evident from the IV curves of the P^+ implanted device that the current increases with the increase in temperature. The activation energy (Ea) required for carrier conduction was determined by linear approximation of "(4)"[40].

$$\sigma_s = \sigma_o \, e^{\frac{E_a}{KT}} \tag{4}$$

Where σ_s is the conductivity at temperature 'T', 'Ea' is the activation energy, 'K' is the Boltzman constant ($= 8.617 \times 10^{-5}$ eV/K) and 'T' is the temperature in Kelvin. Fig. 10 shows the activation energy values for each device. The P^+-implanted device exhibited significantly higher activation energy, indicating that carriers require more energy to become electrically active compared to other devices. This finding aligns with the current-voltage curves. Fig. 11 shows the direct relation between activation energies and resistance of the devices. Higher resistance corresponds to greater energy requirements for electrical conductivity. The fabricated and implanted devices contain different defects and trap levels within the band gap, leading
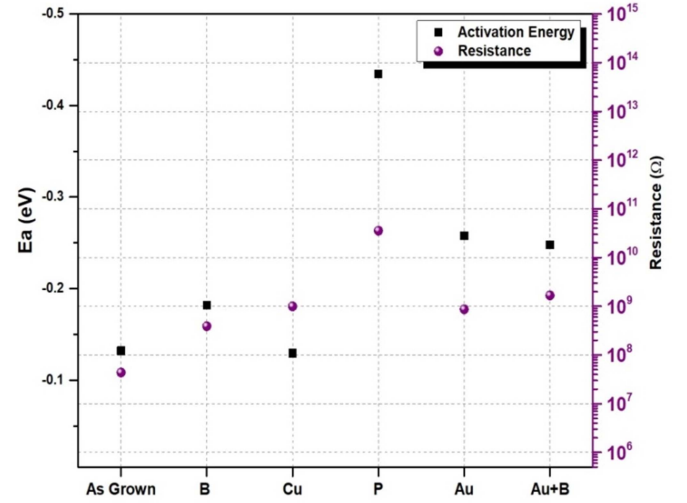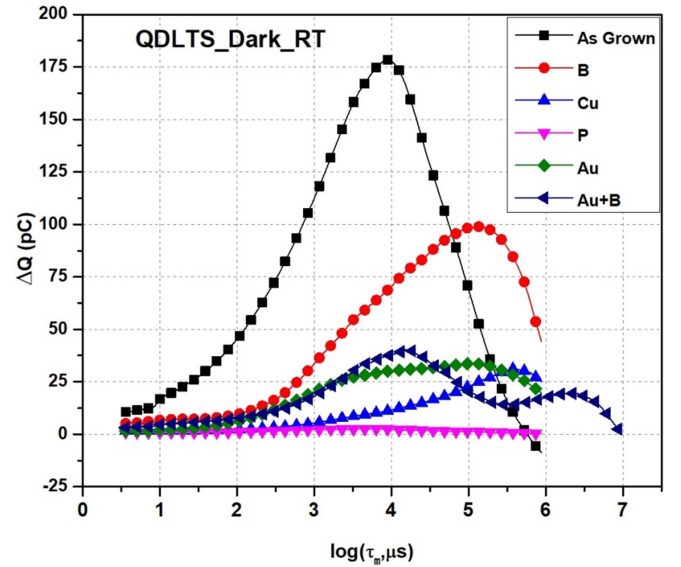

Fig. 12. QDLTS Spectra of as-grown and implanted devices under the no-light condition.

to metastable states. To investigate the density and localization of these traps, Charge Deep Level Transient Spectroscopy (Q-DLTS) was employed. This technique estimates the quality and quantity of traps by measuring the transients of trapped charges during electric field interruptions [14], [41]. The QDLTS spectra plotted in Fig. 12 at room temperature, show the change in charge (ΔQ) as a function of the rate window(τ). This behavior can be described by "(5)" and "(8)" [14], [41], [42].

$$\tau = \frac{t_2 - t_1}{ln\left(t_2/t_1\right)} = \frac{t_1\left(\alpha - 1\right)}{ln\left(\alpha\right)} \tag{5}$$

In this equation, 't_1' is the initial discharge time, 't_2' is the final discharge time, and 'τ' is the rate window, which is a

function of time, during which charge values are measured and recorded. For minimizing the errors t_1 and t_2 should be perfectly proportional $t_2/t_1 = \alpha$. Charges at initial (t_1) and final (t_2) times can be described as [14], [41]:

$$Q(t_1) = Q_0 \, exp \, (-e_n t_1) \tag{6}$$

$$Q(t_2) = Q_0 \, exp \, (-e_n t_2) \tag{7}$$

$$\Delta Q = Q_{t2} - Q_{t1} \tag{8}$$

$$\Delta Q = Q_0 \, [exp \, (-e_n t_2) - exp \, (-e_n t_1)] \tag{9}$$

Where 'e_n' is the electron emission rate and related as [14], [41], [42], [43]:

$$e_n = \sigma T_n T^2 \left(-\frac{E_T}{kT} \right) \tag{10}$$

Where 'σ' is the capture cross-section, 'T' is the Temperature is Kelvin, 'E_T' is the Trap level Energy, 'K' is Boltzmann constant, and 'T_n' is defined as [14], [41], [44]:

$$T_n = 2(3)^{1/2} \left(\frac{2\pi}{h^2} \right)^{3/2} k^2 m_n \tag{11}$$

Where 'h' is the plank constant and 'm_n' is the effective mass of the electron within the device matrix.

Initially, the devices are tested at 0V external bias and then under different biasing conditions (Vbias) for 10 msec charging time (t_c). This bias is responsible for practically charging the trap centers associated with their respective band gaps. When the bias is removed its value decreases from V_{bias} to 0V, during this time (discharge time) charge collected by the trap centers is released and recorded between two-time intervals i.e., initial discharge time (t_1) and final discharge time (t_2) as referred in "(6)". According to the subject scheme, Q-DLTS spectra are plotted in Fig. 12 (at room temperature) as a function of rate window 'τ'. The quantity of the traps has two attributes i.e., the number of trap centers (either the recombination or the generation one) and the density of the traps. The quality of the traps is their ability to physically attract the free carriers toward the said energy level.

The trap density 'N_T' can be calculated by "(12)" [14].

$$N_T = \frac{4\Delta Q_{\max}}{qAd} \tag{12}$$

Where 'N_T' is Trap density (concentration), '$\Delta Q_{\max}$' is the maximum change in charge, 'q' is an absolute charge ($= 1.6 \times 10^{-19}$ C), 'A' is contact area, and 'd' is the distance between two contacts i.e., 0.2 cm. Fig. 12 shows that the as-grown device exhibited the highest and sharpest peak i.e., signature of the highest trap density followed by the boron implanted device. In contrast, the P^+-implanted device showed the lowest trap density, suggesting an improvement in device parameters. The doubly implanted ($Au^+\&B^+$) device displayed two peaks. The as-grown device has the narrowest FWHM, reflecting the pure nature of the device, while, the P^+-implanted device showed a broad spectrum with minimal intensity.

To examine the quality and quantity of traps present in the devices characterization was employed from room temperature
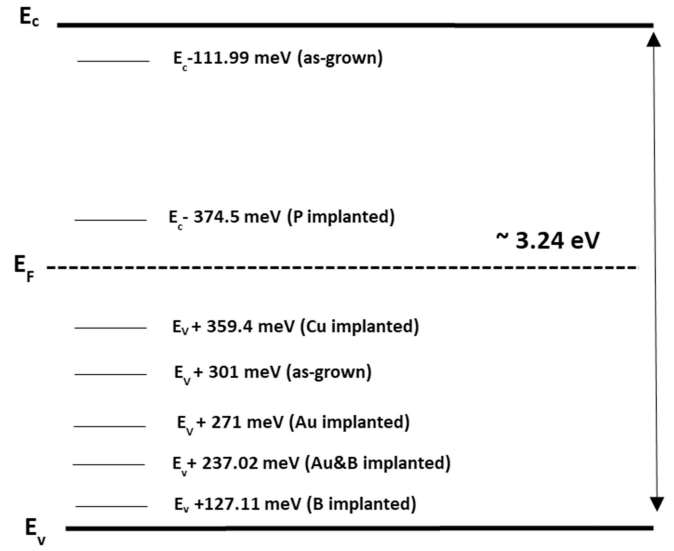

Fig. 13. Band diagram of pristine and implanted ZnO device matrix.

(RT) to 350 K. Trap-assisted activation energy 'E_T' was calculated for each device by linear approximation of (10). The pristine ZnO device exhibited two traps with E_T values $E_v + 301$ meV and $E_c - 312$ meV. However, when ion implantation was performed on the devices with selected ions at a fixed dose of $1 \times 10^{+14}$ cm^{-2} and energy of 400 keV, additional damage and defects were introduced within the ZnO band gap. Different trap levels were expected due to varying band gaps associated with the ZnO device matrix and the relative atomic masses of the implanted ions. The QDLTS analysis provided the trap-assisted energies, which are reported in Table III. The as-grown and implanted devices exhibited trap levels within the band gap. These traps could be of a generation nature or recombination nature. Trap levels above the Fermi level (E_F) and near the conduction band (E_C) act as generation centers, while those below the E_F are of a recombination nature, contributing to leakage current. The complete band picture can be seen in Fig. 13.

This characterization and understanding of trap levels and their nature within the ZnO devices are crucial for optimizing the performance of optoelectronic devices based on ZnO and mitigating issues such as leakage current. The reported trap-assisted parameters provide valuable information for the design and improvement of ZnO-based devices.

As can be seen from the above band picture, the pristine device has two trap levels, one near to conduction band edge and the other near to valance band. When phosphorus is implanted into this device, the trap level shifted deep into the device, i.e., towards the fermi level with a capture cross section (σ_{T1}) of 5.07E-31 cm^2. Under the light condition, the free charge carriers will be generated and will try to surpass this trap level, as soon as these free carriers will cross the fermi level, there is a possibility of getting captured by this trap. Hence, it is expected that the P^+-implanted device will need some external thrust, to be opto-electrically activated. The B^+-implanted device has a trap level very close to the valance band edge, with a capture cross-section

TABLE III
EA, ET AND CAPTURE CROSS-SECTION

Sr. No	Case	Ea_IV (meV)	Ea_error	E_{T1} (meV)	Ea_error	σ_{T1} (cm²)	σ_{T1}_error	E_{T2} (meV)	Et_error	σ_{T2} (cm²)	σ_{T2}_error
1	As depo	-132.09	0.11	Ev+301	0.46	5.2E-20	1.51	Ec-111.99	0.20	1.71E-26	0.60
2	B impl	-181.76	0.16	Ev+127	0.08	2.93E-24	0.25	--	--	--	--
3	Cu impl	-129.29	0.11	Ev+359	0.30	9.08E-21	0.95	--	--	--	--
4	P impl	-434.44	0.28	Ec-374.5	0.79	5.07E-31	2.48	--	--	--	--
5	Au impl	-257.49	0.32	Ev+271	0.11	1.35E-21	0.34	--	--	--	--
6	Au&B impl	-247.74	0.24	Ev+237	0.22	2.29E-21	0.71	--	--	--	--
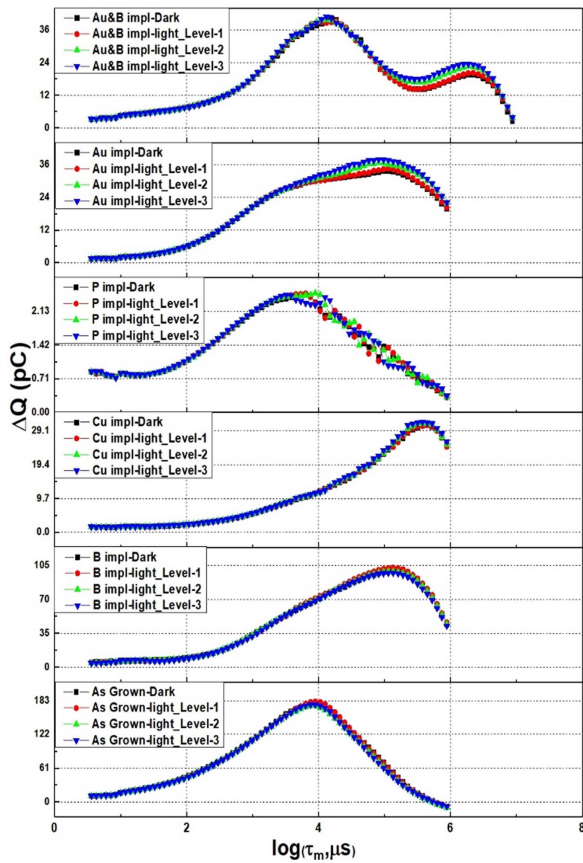
Fig. 14.   QDLTS at varying light intensity for as-grown and implanted ZnO devices.

Fig. 15.   Transients of photovoltage under light and dark conditions at 5 V.

of 2.93E-24 cm², any free charge carriers may recombine at this trap energy and may result in undesirable leakage current. The as–grown device has provided two trap levels which might be clarified, however, in QDLTS the examination of trap levels depends on the evaluation of $\Delta Q \sim$ rate window at a range of temperatures i.e., one has chosen the temperature of 290 K to 350 K. In a given range one has evaluated two linear fits that direct two different trap levels.

The devices were also subjected to varying intensity light at a 5 V applied bias to study the effect of light, as shown in Fig. 14.
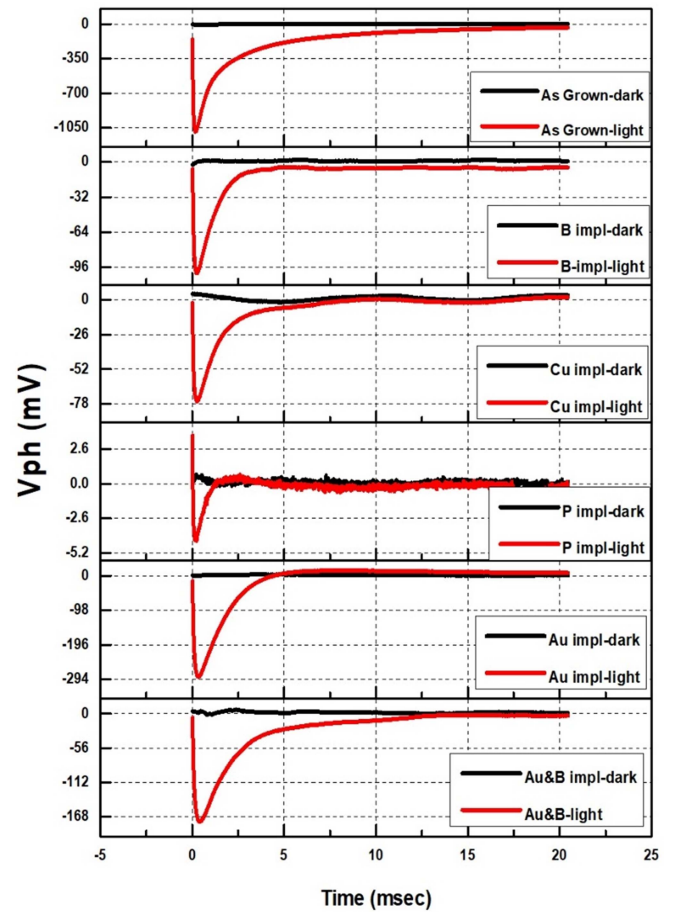
It is revealed that light intensity directly relates to the peak of the QDLTS spectrum in all the devices. The optoelectronic activation was examined in both photo voltaic (PV) mode (no external bias is applied) and photoconductive (PC) mode (with external bias). In PC mode, the devices were subjected to a short pulse of light, and the transient behavior of the photovoltage was observed. The initial drop in photovoltage corresponded to electron-hole pair recombination, followed by a slower decay due to carrier emission [45]. The as-grown device exhibited
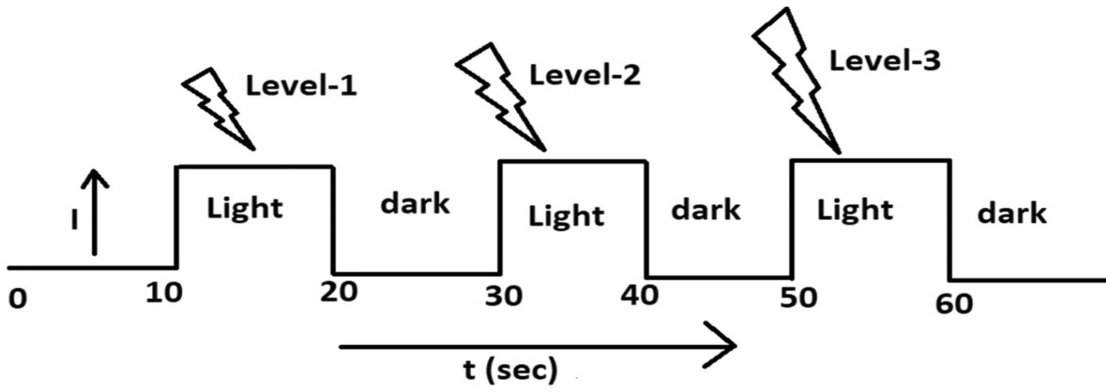
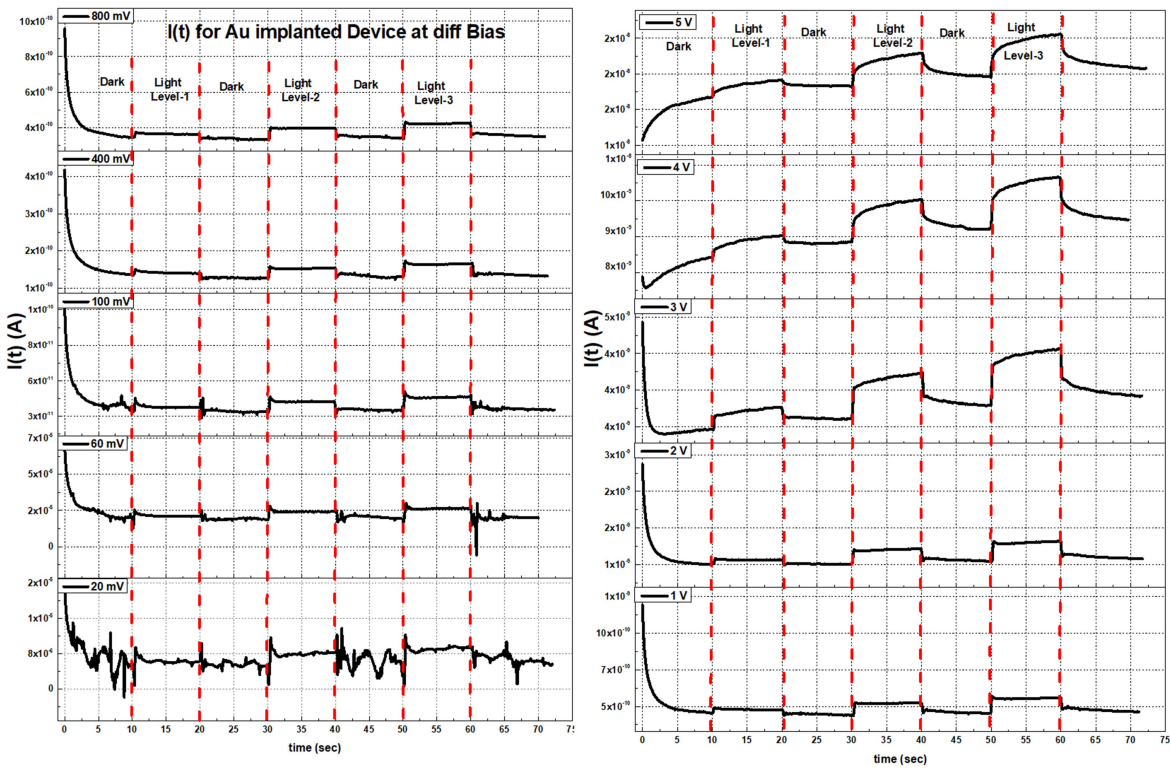Fig. 16.   Schematics of kinetics of photocurrent.

Fig. 17.   Kinetics of photocurrent for Au implanted device at various biases.

the longest decay time, while the P$^+$-implanted device showed the shortest fall time, suggesting improved device-switching capabilities. For photoconductive mode, devices were tested at different V$_{bais}$. Transients of Photo Voltage (TPV) spectra for pristine and implanted ZnO devices in PC mode (V$_{bias}$ of 5 V) are shown in Fig. 15. It is evident that in all cases, light has a profound effect on the subject devices. There is nearly zero voltage available under dark conditions (shown in black), when light impinges on the devices for a very short pulse depending upon the device matrix. The intensity of the peak (red), corresponds to the number of free carriers generated, the time taken by the carriers to approach this intensity corresponds to rise time, and

the time taken by the carriers to diminish (FWHM), corresponds to fall time. The as-grown device has shown the greatest decay time, while P$^+$-implanted device has the lowest fall time, hence less delay By improving the subject device matrix, fast switching can be achieved. By carefully examining the QDLTS data, the following observations were made:

1) *Trap Levels:* The pristine ZnO device had two trap levels, one near the conduction band edge (Ev+301 meV) and the other near the valance band (Ec-312 meV). Ion implantation introduced further trap levels within the ZnO band gap, which varies based on the implanted ions. For example, phosphorus implantation shifted the trap level
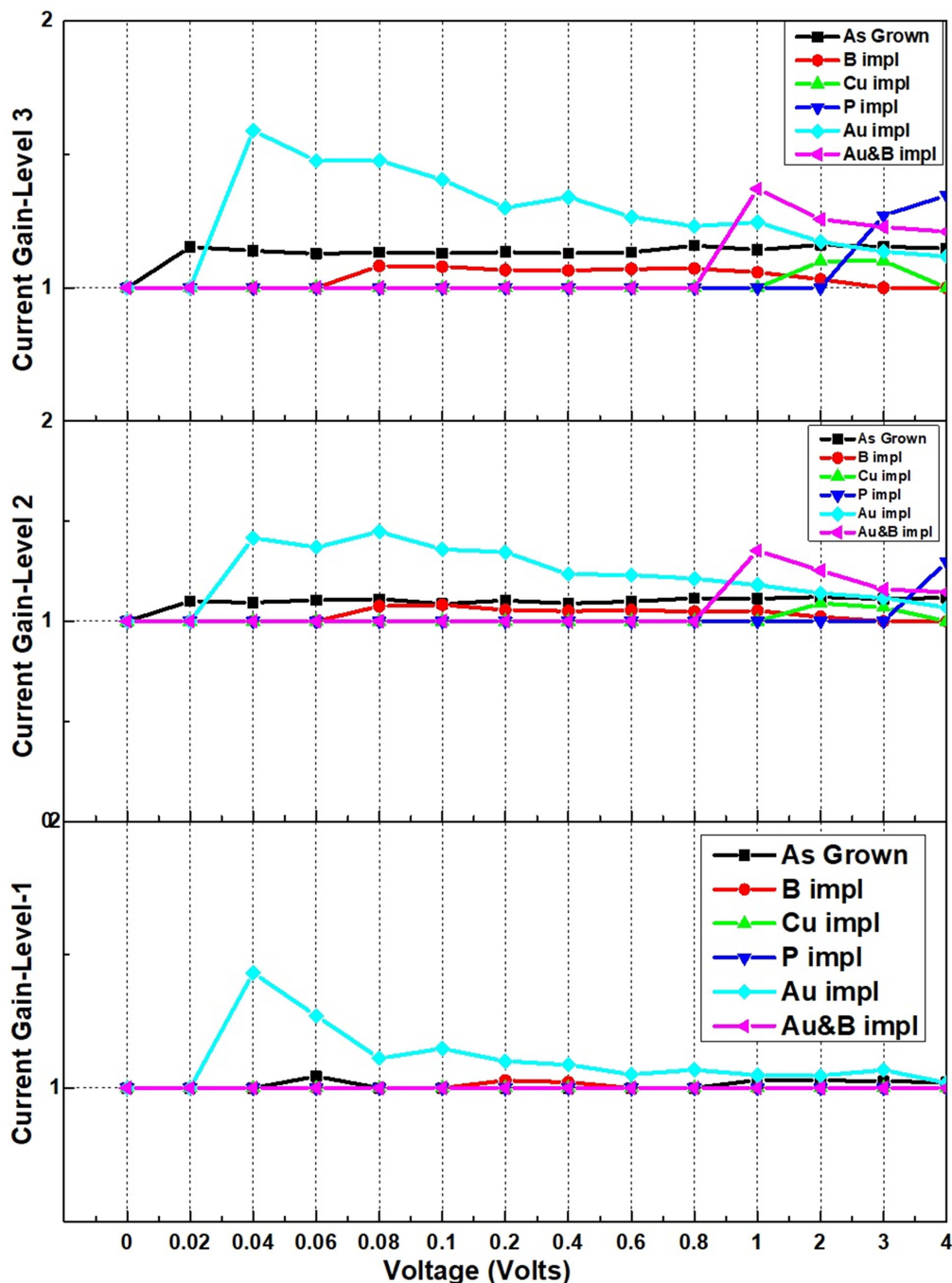
Fig. 18. Current gains at varying light intensity.

deeper into the device, closer to the Fermi level, indicating the need for external thrust to activate optoelectronic behavior. B^+-implantation resulted in a trap level close to the valance band, potentially leading to undesirable leakage current.

2) *Trap Parameters:* The trap-assisted parameters, including capture cross section and trap level energies, were determined through QDLTS analysis. The capture cross-section (σ_{T1}) for the P^+-implanted device was measured to be 5.07E-31 cm^2, while for the B^+-implanted device, it was

2.93E-24 cm^2. These parameters provide insights into the ability of traps to capture free charge carriers and influence device behavior.

3) *Opto-electronic Activation:* The behavior of the devices was examined in both photovoltaic mode (PV) (no external bias) and photoconductive (PC) mode (with external bias). In PC mode, the devices were subjected to a short pulse of light, and the transient behavior of the photovoltage was observed. The initial drop in photovoltage corresponded to electron-hole pair recombination, followed by a slower

decay due to carrier emission. The as-grown device exhibited the longest decay time, while the P^+-implanted device showed the shortest fall time, suggesting improved device switching capabilities. The kinetics of current under dark and luminous conditions was investigated at various applied voltages and light intensities. The measurements involved subjecting the devices to dark conditions for 10 seconds and then exposing them to light for the next 10 seconds at different potential and light intensity levels such that level-1<level-2<level-3. The schematic is shown in Fig. 16. It was observed that, as the bias potential increased, both the dark and photocurrent levels increased. Furthermore, the different light intensities resulted in varying current levels, as the light intensity increases more carriers are generated, resulting in higher current levels at higher light intensity levels. The current level under dark is lower due to absence of photo-generated carriers. This phenomenon is illustrated in Fig. 17 for the Au^+-implanted device.

The current gains of the as-grown and implanted ZnO devices were determined using "(13)" and plotted in Fig. 18 at various applied voltages and light intensity levels.

$$current\ gain\ = \frac{I_{light}}{I_{dark}} \quad (13)$$

Based on these results, several observations can be made:

1) *Au^+-Implanted Device:* The Au^+-implanted device exhibited the highest current gain of approximately 1.6 at an applied bias of 40 mV for all intensity levels. However, as the applied potential increased, the gain decreased smoothly. This suggests that the Au^+ implantation introduced trap levels that significantly interacted with light, resulting in a high current gain compared to other cases.

2) *Dual Implantation (Au^+&B^+) Device:* The dually implanted device (Au^+&B^+) showed the highest gain at around 1 V applied potential. This indicates that the combination of Au^+ and B^+ implantation introduced trap levels that contributed to an increased current gain compared to individual implantations.

3) *P^+-Implanted Device:* The P^+-implanted device exhibited the lowest trap density, which could potentially result in a high current gain. However, Fig. 18 suggests that the current gain for P^+ implants may not be significant, possibly due to trap density being independent of light-matter interaction. It is worth noting that the device structure can also influence the numerical gains in ZnO photodetectors. Other researchers, such as Panda and Jacob, have reported a current gain of approximately 2 for annealed ZnO thin films at 300 °C [30]. However, as-grown films in their study did not exhibit any gain. Pon, V.D et al. tested neodymium-doped ZnO thin films at different doping concentrations and observed highest responsivity of 0.73 A/W [46]. This indicates that the specific device structure and processing conditions can play a role in determining the current gains observed in ZnO-based photodetectors.

IV. CONCLUSION

This study focused on the fabrication and characterization of magnetron sputtered ZnO device structures on n-type Si substrates, followed by implantation with various ions. The devices underwent comprehensive analysis to understand their structural, morphological, optical, and electrical properties. Simulation of ions using SRIM/TRIM & SUSPRE guided the selection of viable implant parameters for device processing. XRD analysis confirmed that the crystalanity of the ZnO films was maintained with a preferred <100> orientation after each implantation routine. Among them Au^+ implantation resulted in the highest light extinction within the ZnO matrix, indicating its potential for efficient light-matter interaction and electron-hole pair generation. Photoluminescence analysis revealed that Au^+ implantation exhibited the highest intensity at a wavelength of 435 nm. Electrical resistivity measurements using the current-voltage technique indicated that P^+ implantation significantly damaged the ZnO lattice. The activation energy (E_a) revealed that P^+ implantation required the highest energy for electrical conduction within the device regions. The charge-based deep-level transient spectroscopy analysis was conducted to investigate the quality and quantity of electronic traps introduced by each implantation scheme. The results were used to assess charge relaxation under different drift biases and light intensities, and an energy band diagram was constructed to localize the trap energies within the ZnO's energy gap. Transients of photovoltage and kinetics of dark and photo current were studied under different biases and light intensities to understand the light current behavior of the implanted ZnO devices. The calculated light/dark current ratios provided insights into the responsivity of each implantation scheme, with Au^+-implanted devices exhibiting sharp turn-on and turn-off timings, making them suitable candidates for high bandwidth operation. The results presented in this study may contribute to the understanding of trap levels, light-matter interaction, and current gain in the context of photodetectors, paving the way for future research and advancements in the this field.

REFERENCES

[1] M. Zheng et al., "ZnO ultraviolet photodetectors with an extremely high detectivity and short response time," *Appl. Surf. Sci.*, vol. 481, pp. 437–442, 2019.

[2] P. V. Kamat, "Quantum dot solar cells. Semiconductor nanocrystals as light harvesters," *J. Phys. Chem. C*, vol. 112, pp. 18737–18753, 2008.

[3] Z. R. Rivera, A. M. Alvarez, and M. D. L. L. O. Amador, "Effect of thickness on photocatalytic properties of ZnO thin films deposited by RF magnetron sputtering," in *Proc. IEEE 16th Int. Conf. Elect. Eng., Comput. Sci. Autom. Control*, 2019, pp. 1–6.

[4] A. Zia, N. Shah, S. Ahmed, and E. Khan, "The influence of cobalt on the physical properties of ZnO nanostructures," *Physica Scripta*, vol. 89, 2014, Art. no. 105802.

[5] M. Zamfirescu, A. Kavokin, B. Gil, G. Malpuech, and M. Kaliteevski, "ZnO as a material mostly adapted for the realization of room-temperature polariton lasers," *Phys. Rev. B*, vol. 65, 2002, Art. no. 161205.

[6] Ü. Özgür, D. Hofstetter, and H. Morkoc, "ZnO devices and applications: A review of current status and future prospects," *Proc. IEEE*, vol. 98, no. 7, pp. 1255–1268, Jul. 2010.

[7] Y.-H. Zhang et al., "Ultra-sensitive triethylamine sensors based on oxygen vacancy-enriched ZnO/SnO 2 micro-camellia," *J. Mater. Chem. C*, vol. 9, pp. 6078–6086, 2021.

[8] S. Mondal and D. Basak, "Photophysical investigation of the formation of defect levels in P doped ZnO thin films," *Ceram. Int.*, vol. 48, pp. 20000–20009, 2022.

[9] T. Zhang et al., "Multi-component ZnO alloys: Bandgap engineering, hetero-structures, and optoelectronic devices," *Mater. Sci. Eng.: R: Rep.*, vol. 147, 2022, Art. no. 100661.

[10] A. Zia, S. Ahmed, N. Shah, M. Anis-ur-Rehman, E. Khan, and M. Basit, "Consequence of cobalt on structural, optical and dielectric properties in ZnO nanostructures," *Physica B: Condens. Matter*, vol. 473, pp. 42–47, 2015.

[11] A. Zia, S. Ahmed, and N. Shah, "Investigation of the sensing mechanism in cobalt doped ZnO matrix based on structural, morphology, optical and electrical studies," *J. Optoelectron. Adv. Mater.*, vol. 20, pp. 180–187, 2018.

[12] A. Zia, S. Ahmed, N. Shah, and E. Khan, "Photo electrical and optical anomaly in ferromagnetic cobalt doped ZnO nanostructures," *Physica Scripta*, vol. 90, 2015, Art. no. 065503.

[13] A. Zia, S. Ahmed, and M. Ali, "Defects anomaly in cobalt-doped ZnO nanostructures using optical and charge transient analysis," *Chin. J. Phys.*, vol. 58, pp. 159–165, 2019.

[14] M. Ali, S. Ahmed, F. Younus, and Z. Ali, "Electrical, charge transients and photo response study of as-deposited and phosphorus implanted Cd1-xZnxTe devices for PV applications," *Radiat. Phys. Chem.*, vol. 166, 2020, Art. no. 108498.

[15] A. Das and D. Basak, "Efficacy of ion implantation in zinc oxide for optoelectronic applications: A review," *Amer. Chem. Soc. Appl. Electron. Mater.*, vol. 3, no. 9, pp. 3693–3714, 2021.

[16] A. Turos, P. Jóźwik, M. Wójcik, J. Gaca, R. Ratajczak, and A. Stonert, "Mechanism of damage buildup in ion bombarded ZnO," *Acta Materialia*, vol. 134, pp. 249–256, 2017.

[17] A. Y. Azarov, A. Hallén, X. Du, P. Rauwel, A. Y. Kuznetsov, and B. Svensson, "Effect of implanted species on thermal evolution of ion-induced defects in ZnO," *J. Appl. Phys.*, vol. 115, 2014, Art. no. 073512.

[18] A. Y. Azarov, E. Wendler, A. Y. Kuznetsov, and B. Svensson, "Crucial role of implanted atoms on dynamic defect annealing in ZnO," *Appl. Phys. Lett.*, vol. 104, 2014, Art. no. 052101.

[19] A. Azarov, L. Vines, P. Rauwel, E. Monakhov, and B. G. Svensson, "Silver migration and trapping in ion implanted ZnO single crystals," *J. Appl. Phys.*, vol. 119, 2016.

[20] Y. G. Fedorenko, "Ion-beam-induced defects," in *CMOS Technology: Methods of Study*. London, U.K.: IntechOpen, 2017.

[21] C.-K. Lew, B. Johnson, and J. McCallum, "Deep level transient spectroscopy study of heavy ion implantation induced defects in silicon," *J. Appl. Phys.*, vol. 124, 2018, Art. no. 125701.

[22] T. Wu et al., "Evolution of native defects in ZnO nanorods irradiated with hydrogen ion," *Sci. Rep.*, vol. 9, 2019, Art. no. 17393.

[23] B. Kafle, S. Acharya, S. Thapa, and S. Poudel, "Structural and optical properties of Fe-doped ZnO transparent thin films," *Ceram. Int.*, vol. 42, pp. 1133–1139, 2016.

[24] L. Xu and X. Li, "Influence of Fe-doping on the structural and optical properties of ZnO thin films prepared by sol–gel method," *J. Cryst. Growth*, vol. 312, pp. 851–855, 2010.

[25] M. Yarahmadi, H. Maleki-Ghaleh, M. E. Mehr, Z. Dargahi, F. Rasouli, and M. H. Siadati, "Synthesis and characterization of Sr-doped ZnO nanoparticles for photocatalytic applications," *J. Alloys Compounds*, vol. 853, 2021, Art. no. 157000.

[26] R. Anugrahwidya, N. Yudasari, and D. Tahir, "Optical and structural investigation of synthesis ZnO/Ag nanoparticles prepared by laser ablation in liquid," *Mater. Sci. Semicond. Process.*, vol. 105, 2020, Art. no. 104712.

[27] W. Wang, Y. Liu, J. Ma, Y. Wang, X. Peng, and J. He, "Effects of annealing temperature on the properties of ZnO thin films and ultraviolet photodetectors," in *Proc. IEEE Int. Conf. Electron Devices Solid-State Circuits*, 2019, pp. 1–3.

[28] S. K. Sen et al., "X-ray peak profile analysis of pure and Dy-doped α-MoO3 nanobelts using Debye-Scherrer, Williamson-Hall and Halder-Wagner methods," *Adv. Natural Sci.: Nanoscience Nanotechnol.*, vol. 11, 2020, Art. no. 025004.

[29] M. Shkir, "Enhancement in optical and electrical properties of ZnO thin films via Co doping for photodetector applications," *Mater. Sci. Eng.: B*, vol. 284, 2022, Art. no. 115861.

[30] S. Panda and C. Jacob, "Preparation of transparent ZnO thin films and their application in UV sensor devices," *Solid-State Electron.*, vol. 73, pp. 44–50, 2012.

[31] M. S. Samuel, L. Bose, and K. George, "Optical properties of ZnO nanoparticles," *Academic Rev.*, vol. 16, pp. 57–65, 2009.

[32] A. López-Suárez, D. Acosta, C. Magaña, and F. Hernández, "Optical, structural and electrical properties of ZnO thin films doped with Mn," *J. Mater. Sci.: Mater. Electron.*, vol. 31, pp. 7389–7397, 2020.

[33] P. Y. Dave, K. H. Patel, K. V. Chauhan, A. K. Chawla, and S. K. Rawal, "Examination of zinc oxide films prepared by magnetron sputtering," *Procedia Technol.*, vol. 23, pp. 328–335, 2016.

[34] M. Mishra, S. Sushama, S. K. Pandey, and S. Chakrabarti, "Phosphorus doping of ZnO using spin-on dopant process: A better choice than costly and destructive ion-implantation technique," *J. Lumin.*, vol. 233, 2021, Art. no. 117921.

[35] S. H. Bae, S. Y. Lee, H. Y. Kim, and S. Im, "Effects of post-annealing treatment on the light emission properties of ZnO thin films on Si," *Opt. Mater.*, vol. 17, pp. 327–330, 2001.

[36] J. Hu, X. Ma, Z. Xie, N. Wong, C. Lee, and S. Lee, "Characterization of zinc oxide crystal whiskers grown by thermal evaporation," *Chem. Phys. Lett.*, vol. 344, pp. 97–100, 2001.

[37] A. Cetin et al., "Optical properties of Cu implanted ZnO," *Nucl. Instrum. Methods Phys. Res. Sect. B: Beam Interact. Mater. At.*, vol. 249, pp. 474–477, 2006.

[38] T. Karali et al., "Optical properties and luminescence of metallic nanoclusters in ZnO: Cu," *Physica B: Condens. Matter*, vol. 363, pp. 88–95, 2005.

[39] M. Singh et al., "Room temperature photoluminescence and spectroscopic ellipsometry of reactive co-sputtered Cu-doped ZnO thin films," *Optik*, vol. 257, 2022, Art. no. 168860.

[40] L. Jentjens, N. Raeth, K. Peithmann, and K. Maier, "Electrical conductivity and asymmetric material changes upon irradiation of Mg-doped lithium niobate crystals with low-mass, high-energy ions," *J. Appl. Phys.*, vol. 109, 2011, Art. no. 124104.

[41] S. Hassan, S. Ahmed, M. Ali, and S. Fahad, "Advanced electrical characterization of AlN/Si based heterogeneous junction for photonic applications," *Mater. Sci. Semicond. Process.*, vol. 138, 2022, Art. no. 106292.

[42] J. B. Rothenberger, D. E. Montenegro, M. A. Prelas, T. K. Ghosh, R. V. Tompson, and S. K. Loyalka, "A Q-DLTS investigation of aluminum nitride surface termination," *J. Mater. Res.*, vol. 27, pp. 1198–1204, 2012.

[43] L. Wang et al., "The mechanism of persistent photoconductivity induced by minority carrier trapping effect in ultraviolet photo-detector made of polycrystalline diamond film," *Thin Solid Films*, vol. 520, pp. 752–755, 2011.

[44] C. Lee et al., "Performance and defects in phosphorescent organic light-emitting diodes," *Solid State Sci.*, vol. 12, pp. 1873–1876, 2010.

[45] D. K. Schroder, *Semiconductor Material and Device Characterization*. Hoboken, NJ, USA: Wiley, 2015.

[46] I. L. P. Raj et al., "Enhancement of optoelectronic parameters of Nd-doped ZnO nanowires for photodetector applications," *Opt. Mater.*, vol. 109, 2020, Art. no. 110396.